A parametric scheme for the retrieval of two-dimensional ocean wave spectra from synthetic aperture radar look cross spectra

J. Schulz-Stellenfleth

Remote Sensing Technology Institute, German Aerospace Center (DLR), Oberpfaffenhofen, Germany

S. Lehner

Rosenstiel School of Marine and Atmospheric Science, University of Miami, Miami, Florida, USA

D. Hoja

Remote Sensing Technology Institute, German Aerospace Center (DLR), Oberpfaffenhofen, Germany

Received 25 November 2004; revised 14 February 2005; accepted 21 February 2005; published 7 May 2005.

[1] A parametric inversion scheme for the retrieval of two-dimensional (2-D) ocean wave spectra from look cross spectra acquired by spaceborne synthetic aperture radar (SAR) is presented. The scheme uses SAR observations to adjust numerical wave model spectra. The Partition Rescaling and Shift Algorithm (PARSA) is based on a maximum a posteriori approach in which an optimal estimate of a 2-D wave spectrum is calculated given a measured SAR look cross spectrum (SLCS) and additional prior knowledge. The method is based on explicit models for measurement errors as well as on uncertainties in the SAR imaging model and the model wave spectra used as prior information. Parameters of the SAR imaging model are estimated as part of the retrieval. Uncertainties in the prior wave spectrum are expressed in terms of transformation variables, which are defined for each wave system in the spectrum, describing rotations and rescaling of wave numbers and energy as well as changes of directional spreading. Technically, the PARSA wave spectra retrieval is based on the minimization of a cost function. A Levenberg-Marquardt method is used to find a numerical solution. The scheme is tested using both simulated SLCS and ERS-2 SAR data. It is demonstrated that the algorithm makes use of the phase information contained in SLCS, which is of particular importance for multimodal sea states. Statistics are presented for a global data set of 11,000 ERS-2 SAR wave mode SLCS acquired in southern winter 1996.

Citation: Schulz-Stellenfleth, J., S. Lehner, and D. Hoja (2005), A parametric scheme for the retrieval of two-dimensional ocean wave spectra from synthetic aperture radar look cross spectra, *J. Geophys. Res.*, *110*, C05004, doi:10.1029/2004JC002822.

1. Introduction

[2] Spaceborne synthetic aperture radar (SAR) is still the only instrument providing two-dimensional (2-D) spectral information on a global and continuous basis. SAR data as acquired by the European Remote Sensing Satellite 2 (ERS-2) or the Environmental satellite (ENVISAT) launched in 1995 and 2002 respectively are particularly valuable for the assimilation of numerical ocean wave forecast models. Today's operational forecast systems run at various weather centers have reached a level of accuracy where further improvements seem to require the use of more detailed spectral information only available from SAR so far.

[3] The first proposed SAR wave measurements techniques were based on single ‘‘frozen’’ SAR images [*Hasselmann et al.*, 1996; *Krogstad et al.*, 1994]. Different algorithms for the inversion of the respective SAR image variance spectra were developed and it was demonstrated that these data contain useful information on the 2-D ocean wave spectrum [*Heimbach et al.*, 1998]. A more advanced approach is based on the use of SAR look cross spectra (SLCS), which enable the resolution of wave propagation direction ambiguities and which have lower noise levels [*Engen and Johnsen*, 1995]. Furthermore approaches to estimate sea surface elevation fields in the spatial domain from complex SAR data have been proposed recently [*Schulz-Stellenfleth and Lehner*, 2004]. Although the SLCS technique has been known for a longer time now, the operational availability of SLCS from the ENVISAT ASAR has caused new interest in the method in particular among the ocean wave modeling community.

[4] This paper is concerned with a rigorous statistical treatment of the SLCS inversion problem, i.e., the estimation of 2-D ocean wave spectra dealing with the SLCS distortions and the information loss caused by the nonlinear

0148-0227/05/2004JC002822$09.00

SAR imaging mechanism as, e.g., described by *Engen and Johnsen* [1995]. The approach is geared toward the retrieval of complete 2-D wave spectra and is thus different to the methods, e.g., described by *Chapron et al.* [2001] and *Engen et al.* [2001], where the SAR measurement is restricted to the long wave regime.

[5] The type of retrieval problem described above is very common in remote sensing and is usually solved by using some a priori information from other sources like, e.g., models or other sensors. Attempts to find solutions without prior information have been made [*Lyzenga*, 2002; *Engen and Johnson*, 1995]. These approaches are restricted to the long wave regime and the missing regularization makes it more difficult to retrieve realistic wave spectra. For conventional SAR image variance spectra different approaches have been proposed to blend SAR measurement and prior knowledge. *Hasselmann et al.* [1996] and *Krogstad et al.* [1994] used model spectra as prior information, whereas *Mastenbroek and de Valk* [2000] took collocated ERS-2 scatterometer measurements as additional input. Several studies showing the performance of the schemes have been carried out [*Heimbach et al.*, 1998; *Mastenbroek and de Valk*, 2000; *Breivik et al.*, 1998].

[6] A first very general study on the SLCS inversion problem using prior knowledge was presented by *Dowd and Vachon* [2001]. The study contains no statistical analysis and the proposed scheme obviously has a problem with discontinuities of the retrieved spectra at the azimuthal cut-off wave number. As will be shown the scheme presented in this paper is able to solve this problem using some additional prior assumptions. The method proposed here extends the basic concepts of the inversion scheme introduced by *Hasselmann et al.* [1996], which are as follows: (1) the scheme uses 2-D wave spectra provided by numerical models as a priori information and (2) the method is based on a parameterization of the prior wave spectrum using a partitioning approach. The method described in this paper is referred to as Partition Rescale and Shift Algorithm (PARSA) in the following. It has several additional features compared to the scheme described by *Hasselmann et al.* [1996]: (1) the scheme has the directional spreading of the different wave systems as an additional parameter; (2) the algorithm is based on explicit models for the measurement error, errors in the forward model, and uncertainties in the prior wave spectrum; and (3) the scheme is based on a maximum a posteriori approach. The second iteration loop used by *Hasselmann et al.* [1996], where the prior wave spectrum is adjusted and fed back into the optimal estimation problem is avoided. This approach has two advantages: the sensitive cross assignment procedure used by *Hasselmann et al.* [1996] is not required and based on the rigorous formulation as an optimal estimation problem it is possible to estimate the error covariance of the retrieved parameters: (1) the scheme makes use of the phase information contained in SLCS to resolve ambiguities in the wave propagation direction; (2) the scheme provides estimates for uncertain parameters in the SAR imaging model in addition; and (3) a new partitioning method is used which allows overlapping partitions and thus avoids discontinuities occurring in the inverted catchment algorithm [*Gerling*, 1992] used so far. The design of the PARSA scheme was guided by the requirements of wave model assimilation, which is regarded as the most important application of global SAR data as provided by the ENVISAT ASAR.

[7] The paper is structured as follows. In section 2 a brief introduction to SLCS is given. Section 3 explains the maximum a posteriori approach which is the basis for the PARSA scheme. Models for the measurement error as well as for errors in the forward model and uncertainties in the prior wave spectrum are presented in section 4 as important components of the retrieval procedure. Section 5 is about the numerical retrieval procedure, which is based on a Levenberg-Marquardt method. The discussion includes criteria for the termination of the iteration and the computation of the error covariance matrix for the retrieved wave parameters. In section 6 the performance of the scheme is illustrated using simulated data. In particular, the benefit of the phase information contained in SLCS is demonstrated. In section 7 the PARSA scheme is applied to a global data set of reprocessed ERS-2 SLCS introduced by *Lehner et al.* [2000]. Global maps as well as scatterplots comparing retrieved and prior wave spectra are presented.

2. Synthetic Aperture Radar (SAR) Look Cross Spectra (SLCS)

[8] In this section SLCS are introduced, which are the basis for the PARSA inversion scheme. It is well known that SLCS have the following two advantages compared to conventional SAR image variance spectra [*Engen and Johnsen*, 1995]: (1) SLCS help to resolve the wave propagation direction ambiguities present in symmetric SAR image variance spectra and (2) SLCS have lower noise levels. SLCS are based on two looks which are processed from the azimuth spectrum of complex SAR data [*Engen and Johnsen*, 1995]. The looks show exactly the same area of the sea surface and are separated in time by typically one second. The looks can thus be used to gain information about wave motion and in particular about wave propagation directions. A standard approach to detect the respective phase shifts is to compute the SLCS [*Honerkamp*, 1993], which is defined as the Fourier spectrum of the respective cross covariance function $\rho_{I_\sigma^1 I_\sigma^2}$:

$$\Phi_{\mathbf{k}}^{I_\sigma^1 I_\sigma^2} = \mathcal{F}\left(\rho_{I_\sigma^1 I_\sigma^2}\right). \tag{1}$$

There are different approaches to estimate the cross spectrum from a given measurement [*Honerkamp*, 1993]. The SLCS is a complex valued function with symmetric real and antisymmetric imaginary part. The positive peaks of the imaginary part indicate the propagation direction of the different harmonic wave components. A physical model describing the relationship between ocean wave spectra and SLCS has been derived by *Engen and Johnsen* [1995] and is summarized in Appendix C. Noise properties of SLCS including the impact of estimation errors and speckle noise were analyzed by *Schulz-Stellenfleth and Lehner* [2005].

3. Retrieval Strategy

[9] A big challenge in SAR ocean wave retrieval is the consistent blending of SAR information and respective

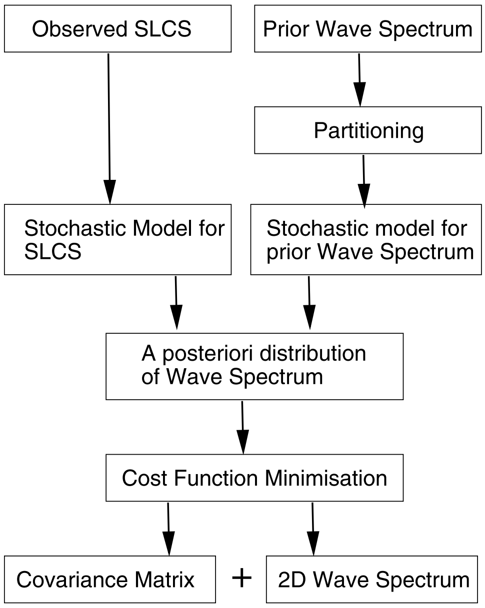

Figure 1. Flowchart of the Partition Rescaling and Shift Algorithm (PARSA) retrieval scheme.

prior knowledge. The strategy followed in this study is based on the so-called maximum a posteriori approach [*Rodgers*, 2000]. The objective of this concept is to maximize the conditional probability of the retrieved wave spectrum given the SLCS and the prior wave spectrum. Using the Bayes theorem this probability can be written as

$$\mathrm{pdf}(F_{\mathbf{k}}, \alpha | \Phi_{\mathbf{k}}) = \frac{\mathrm{pdf}(\Phi_{\mathbf{k}} | F_{\mathbf{k}}, \alpha)\ \mathrm{pdf}(\alpha)\ \mathrm{pdf}(F_{\mathbf{k}})}{\mathrm{pdf}(\Phi_{\mathbf{k}})}, \quad (2)$$

where $\mathrm{pdf}(\Phi_{\mathbf{k}}|F_{\mathbf{k}}, \alpha)$ is conditional distribution of the measured SLCS $\Phi_{\mathbf{k}}$ given an ocean wave spectrum $F_{\mathbf{k}}$ and a forward model, which contains a stochastic parameter vector α, $\mathrm{pdf}(\alpha)$ is the prior distribution of parameters in the forward model, $\mathrm{pdf}(F_{\mathbf{k}})$ is the prior distribution of the ocean wave spectrum $F_{\mathbf{k}}$, and $\mathrm{pdf}(\Phi_{\mathbf{k}})$ is the prior distribution of the SLCS, which is irrelevant for the inversion procedure. The overall structure of the retrieval scheme based on equation (2) is depicted in the flowchart shown in Figure 1. The different components will be explained going from top to bottom, starting with probability models for both SLCS estimation errors and uncertainties in the prior wave spectrum.

4. Error Models

4.1. Measurement Errors

[10] For an optimal wave spectra retrieval it is necessary to quantify the potential errors contained in the SLCS measurement. The analysis by *Schulz-Stellenfleth and Lehner* [2005] showed that real and imaginary part of the estimated SLCS can to first order be regarded as uncorrelated. Standard deviations of the real and imaginary part of the SLCS associated with spectral estimation errors can be estimated based on the SLCS coherence. Denoting the exact SLCS with $\overline{\Phi}_{\mathbf{k}}^{\mathrm{obs}}$, the estimated SLCS is written as

$$\Phi_{\mathbf{k}}^{\mathrm{obs}} = \overline{\Phi}_{\mathbf{k}}^{\mathrm{obs}} + \epsilon_{\mathbf{k}}^{S}, \quad (3)$$

where $\epsilon_{\mathbf{k}}^{S}$ is a zero mean complex Gaussian process with standard deviation given by

$$\mathrm{stdv}\left(\epsilon_{\mathbf{k}}^{S}\right) \approx \frac{|\Phi_{\mathbf{k}}^{I^1 I^2}|}{N_s}\ (0.75, 0.25) =: \left(\sigma_{\mathbf{k}}^{RS}, \sigma_{\mathbf{k}}^{IS}\right). \quad (4)$$

Here, N_s is the number of samples averaged in the SLCS estimation procedure. The chosen values for the standard deviations stem from an analysis carried out by *Schulz-Stellenfleth et al.* [2002] and *Schulz-Stellenfleth and Lehner* [2005] assuming a SLCS coherence of 0.7, which is regarded as typical. It is of course possible to adjust the error model for each spectrum based on the estimated coherence, but to keep the further discussion simple a constant coherence is assumed in the following.

[11] To keep the computational effort low, the PARSA scheme uses a polar grid with logarithmic spacing in the frequency dimension according to

$$k_j = \frac{4\,\pi^2 f_0^2}{g}\ C_0^{2\,(j-1)}\ j = 1, .., n_k, \quad (5)$$

where g is the gravitational acceleration. To make full use of the wavelength range between 20 m and 1000 m covered by the official ENVISAT ASAR SLCS product [*Johnsen et al.*, 2002], a value of f_0 = 0.0395 Hz is chosen for the lowest frequency bin, which is slightly lower than in the standard setup of the wave model WAM with f_0^{WAM} = 0.04177 Hz [*Heimbach et al.*, 1998]. To have a frequency sampling comparable to the WAM model the inversion scheme uses n_k = 25 wave number bins. To cover the high-frequency part of the WAM model, which goes up to 0.41 Hz, one then has to choose C_0 = 1.102405. The grid has n_φ = 36 equally spaced directions, which is in agreement with the grid of the official ENVISAT SLCS product. Figure 2a shows the average number of Cartesian grid points contained in the logarithmic wave number bins assuming that ERS-2 wave mode imagettes are used for the spectral estimation [*Lehner et al.*, 2000]. One can see that for shorter waves the number of averaged spectral bins is so high that the impact of estimation errors on the retrieval (compare equation (4)) becomes negligible. However, for longer swell it has to be taken into account. The fact that there are only few or even none Cartesian grid points in the high-frequency part of the PARSA polar grid is because the respective bins lie partly outside the spectral regime covered by the wave mode imagettes. The exact intervals in the wavelength and frequency domain covered by the bins of the polar grid are shown in Figure 2b.

[12] It is important to note that the ocean wave imaging process is influenced by waves with frequencies higher than 0.41 Hz not contained in the PARSA frequency grid. This is simply due to the fact that these waves contribute significantly to the orbital velocity variance [*Alpers et al.*, 1981; *Lyzenga*, 1986; *Schulz-Stellenfleth and Lehner*, 2002]. To take these waves into account the spectrum is extrapolated

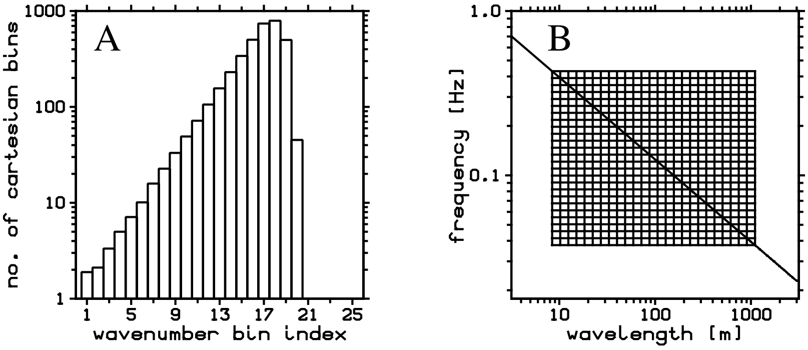

Figure 2. (a) Average number of Cartesian grid points contained in the wave number bins used in the PARSA scheme (compare equation (5)). An image size of 10 by 5 km was assumed corresponding to the ERS wave mode. (b) Respective range of wavelength and frequency for each bin.

assuming a k^{-4} power law [*Phillips*, 1985] as described by *Schulz-Stellenfleth and Lehner* [2002].

4.2. Uncertainties in the SAR Imaging Model

[13] It is well known that the SAR ocean wave imaging model contains significant uncertainties. In particular, the phase and magnitude of the RAR modulation mechanism is known only with low accuracy [*Brüning et al.*, 1994; *Schmidt*, 1995]. This circumstance is only to some degree due to the lack of respective measurements, but there is some indication that the real aperture radar (RAR) modulation mechanism itself has stochastic components [*Schmidt*, 1995].

[14] To take into account uncertainties in the forward model, we assume that the simulated SLCS $\Phi^{\rm sim}$ calculated according to the nonlinear integral transform derived by *Engen and Johnsen* [1995] (compare Appendix C) can deviate from the "true" SLCS denoted by $\overline{\Phi}$. The proposed error model has three components, which refer to different characteristic features of the SLCS and can be written as

$$\overline{\Phi}_{\mathbf{k}} = \alpha_1\ \exp\left[-k_x^2\ \beta^2\ \alpha_2\right]\ \Phi_{\mathbf{k}}^{\rm sim} + \epsilon_{\mathbf{k}}^F. \tag{6}$$

Here, α_1, α_2 and $\epsilon_{\mathbf{k}}^F$ have the following meanings: (1) α_1 is a Gaussian distributed variable with unit mean and standard deviation σ_{α_1}, which describes errors in the overall energy level of the spectrum as, e.g., caused by uncertainties in the magnitude of the RAR MTF; (2) α_2 is a Gaussian distributed variable with zero mean and standard deviation σ_{α_2}, which describes uncertainties in the cut-off wavelength of the forward model; and (3) $\epsilon_{\mathbf{k}}^F$ is additive white Gaussian noise with independent real and imaginary part and zero mean. It is supposed to take into account errors in the fine-scale structure of the SLCS, e.g., caused by errors in the phase of the RAR MTF. For the standard deviation of ϵ^F we assume relative errors for both real and imaginary part of the SLCS, i.e.,

$$\text{stdv}\ \epsilon_{\mathbf{k}}^F = \left(\sigma_{\mathbf{k}}^{\rm RF}, \sigma_{\mathbf{k}}^{\rm IF}\right) = \left(\nu_{\rm RF}\ \max_{\mathbf{k}} |{\rm Re}\Phi_{\mathbf{k}}^{\rm obs}|, \nu_{\rm IF}\ \max_{\mathbf{k}} |{\rm Im}\Phi_{\mathbf{k}}^{\rm obs}|\right). \tag{7}$$

Here, $\nu_{\rm RF}$ and $\nu_{\rm IF}$ denote the expected error in the fine-scale structure of the real and imaginary part expressed as a fraction of the respective maximum values.

[15] Combining the models for estimation errors and uncertainties in the forward model, the conditional probability of the measured SLCS given an ocean wave spectrum $F_{\mathbf{k}}$ and a parameter vector α is given by

$$\begin{aligned} {\rm pdf}(\Phi_{\mathbf{k}}|F_{\mathbf{k}},\alpha) \sim \prod_{\mathbf{k}\in\Pi} \exp&\left[-\frac{\left({\rm Re}\left(\alpha_1\ e^{-k_x^2\ \beta^2\ \alpha_2}\ \Phi_{\mathbf{k}}^{\rm sim} - \Phi_{\mathbf{k}}\right)\right)^2}{2\ \left(\sigma_{\mathbf{k}}^{\rm RF}\right)^2 + 2\ \left(\sigma_{\mathbf{k}}^{RS}\right)^2}\right] \\ \prod_{\mathbf{k}\in\Pi} \exp&\left[-\frac{\left({\rm Im}\left(\alpha_1\ e^{-k_x^2\ \beta^2\ \alpha_2}\ \Phi_{\mathbf{k}}^{\rm sim} - \Phi_{\mathbf{k}}\right)\right)^2}{2\ \left(\sigma_{\mathbf{k}}^{\rm IF}\right)^2 + 2\ \left(\sigma_{\mathbf{k}}^{IS}\right)^2}\right], \end{aligned} \tag{8}$$

where it was assumed that both error contributions are independent. The set of wave number vectors of the half polar grid Π is given by

$$\Pi = \{\mathbf{k}_i \mid 1 \le i \le N\}, \tag{9}$$

with $N = n_k n_\varphi/2$ and the wave number vectors $\mathbf{k}_i$, $i = 1, \ldots, N$ defined according to

$$\begin{aligned} \mathbf{k}_{i\cdot n_k + j} &= \left(k_j\ \cos\left[\frac{2\pi}{n_\varphi}\ i\right], k_j\ \sin\left[\frac{2\pi}{n_\varphi}\ i\right]\right), \qquad 1 \le j \le n_k \\ &0 \le i \le \frac{n_\varphi}{2} - 1. \end{aligned} \tag{10}$$

Here we have assumed that the total number of directional bins n_φ is even.

[16] Table 1 summarizes the standard deviations describing uncertainties in the SLCS model. As the standard deviation defines the 65% confidence interval for a Gaussian distributed variable, it is thus expected, that the given deviations of the parameters from their mean values will be exceeded in about 35% of the cases.

[17] The impact of the exact choice of the standard deviations is very case-dependent. In situations with strong signals in the SLCS the retrieval turned out to be robust with respect to changes of the values. In cases where the retrieval is less dominated by the SAR measurement the impact of the parameters is stronger.

[18] The values given in Table 1 represent estimates of the uncertainties, which are regarded as reasonable. They

Table 1. Standard Deviations of the Parameters α_1, α_2, ν_{RF}, and ν_{IF} Used to Describe Errors in the SAR Ocean Wave Imaging Model (Compare Equation (6))

σ_{α_1}	σ_{α_2}, m^2	$\sigma_{\nu_{RF}}$	$\sigma_{\nu_{IF}}$
0.2	250	0.1	0.1

should be seen as a first guess of more accurate estimates, which are expected from a statistical analysis of the retrieval results.

4.3. Statistical Model for the Ocean Wave Model Spectrum

[19] The prior information needed for the SAR wave spectra retrieval can be either taken from collocated measurements of other sensors [*Mastenbroek and de Valk*, 2000] or from models [*Hasselmann et al.*, 1996; *Krogstad et al.*, 1994]. In the work of *Mastenbroek and de Valk* [2000], ERS scatterometer measurements, which are exactly collocated in time and space with the corresponding wave mode acquisition were used to add the missing information beyond the cut-off wavelength. Although, it is certainly reasonable to use additional and independent measurements, the approach is not followed in this study mainly for two reasons: (1) the most important application of the presented retrieval scheme is the inversion of ASAR wave mode data provided by ENVISAT, which does not carry a scatterometer and (2) the method proposed by *Mastenbroek and de Valk* [2000] is based on a simple parametric JONSWAP type model describing the relation between wind speed U_{10} and the corresponding wind sea. In this study wind sea spectra calculated with a third generation numerical ocean wave model are used as prior information. These spectra are believed to be more realistic, because they contain the best available information about the history of the wind field and the wave dynamics. The approach of this study is to take the overall shape of the spectrum from a numerical ocean wave model and to use the SAR information to adjust parameters like wavelength, wave height, directional spreading and propagation direction. The statistical model used for the prior spectrum is based on the partitioning scheme described in Appendix A, where the spectrum is decomposed into a sum of different wave systems B^i, $i = 1,\ldots, n_p$. In contrast to the method proposed by *Gerling* [1992] the partitions are allowed to overlap, which has the advantage of avoiding discontinuities in cases where partitions are close together.

[20] For the internal calculations the spectral energy values of the wave spectrum $F_\mathbf{k}$ and the respective partitions refer to the cartesian wave number grid, i.e., the unit is m^4. This convention is used for reasons of computational efficiency, because the SAR ocean wave imaging forward model applied several times during the inversion process requires the wave spectrum to be provided in these units. The conversion of $F_\mathbf{k}$ to the standard directional frequency spectrum $F_{f,\varphi}$ with unit m^2 Hz^{-1} rad^{-1} is done by the transformation (assuming deep water)

$$F_{f,\varphi} = \frac{32\,\pi^4 f^3}{g^2}\, F_\mathbf{k}, \tag{11}$$

with gravitational acceleration g.

[21] For each subsystem a stochastic model is used, which prescribes the probability that the energy, the propagation direction, the wavelength, or the directional spreading deviates from the prior spectrum. Using a polar grid (φ, k) for the partitions B^i, the corresponding processes $\tilde{B}^i$ can be written as

$$\tilde{B}^i(\varphi,k) = X_E^i\, X_{\Delta\varphi}\, X_k^i\, B^i\left(\varphi_0^i + \left(\varphi - X_\varphi^i - \varphi_0^i\right)X_{\Delta\varphi}, X_k^i\, k\right) \qquad i = 1,\ldots,n_p, \tag{12}$$

where φ_0^i is the peak direction of the ith partition. The definition of the partition process ensures that rotations, shifts, and changes in the directional spread keep the total energy constant. The variance contribution from the ith partition is thus solely controlled by the parameter X_E^i. Furthermore, the approach of changing the wavelength by rescaling of the wave number ensures that power laws in k, e.g., the k^{-4} high-frequency tail of wind seas [*Phillips*, 1985] is maintained by the transformation.

[22] For a given set of transformation parameters the corresponding spectrum is computed with a bilinear interpolation method, which turned out to give sufficient smooth results. Figure 3 illustrates the different transformations used in the PARSA scheme. The prior spectrum with a single wave system of 250 m wavelength is shown in Figure 3a. The four allowed transformations applied to this system are depicted in Figures 3b–3d. One can see that the wave number rescaling factor of X_k = 1.2 shifts the peak wavelength from 250 m to 300 m. The directional spreading is increased if $X_{\Delta\varphi}$ is less than one 1 and vice versa.

[23] The four transformation parameters for each partition are collected in a vector

$$\hat{\mathbf{X}}^i = \left(X_E^i, X_k^i, X_\varphi^i, X_{\Delta\varphi}^i\right), \quad i = 1,\ldots,n_p, \tag{13}$$

which is assumed to be Gaussian distributed with independent components. The mean is given by

$$\boldsymbol{\nu}^i = \langle\hat{\mathbf{X}}^i\rangle = (1,1,0,1) \quad i = 1,..,n_p, \tag{14}$$

and the standard deviation is defined as

$$\mathrm{stdv}\left(\hat{\mathbf{X}}^i\right) = \left(\sigma_E^i, \sigma_k^i, \sigma_\varphi^i, \sigma_{\Delta\varphi}^i\right) \quad i = 1,..,n_p. \tag{15}$$

As the different partition processes are assumed to be independent, the prior wave spectrum can be expressed as

$$\tilde{F}\left(\hat{\mathbf{X}}^\mathbf{1},\ldots,\hat{\mathbf{X}}^{\mathbf{n_p}}\right) = \sum_{i=1}^{n_p} \tilde{B}^i\left(\hat{\mathbf{X}}^i\right). \tag{16}$$

In summary, the prior pdf of the wave spectrum can be written as

$$\mathrm{pdf}(F) = \mathrm{pdf}\left(\overline{\mathbf{X}}\right) \sim \prod_{i=1}^{4\,n_p} \exp\left[-\frac{\left(\overline{\mathbf{X}}_i - \overline{\boldsymbol{\nu}}_i\right)^2}{2\,\overline{\boldsymbol{\sigma}}_i^2}\right], \tag{17}$$

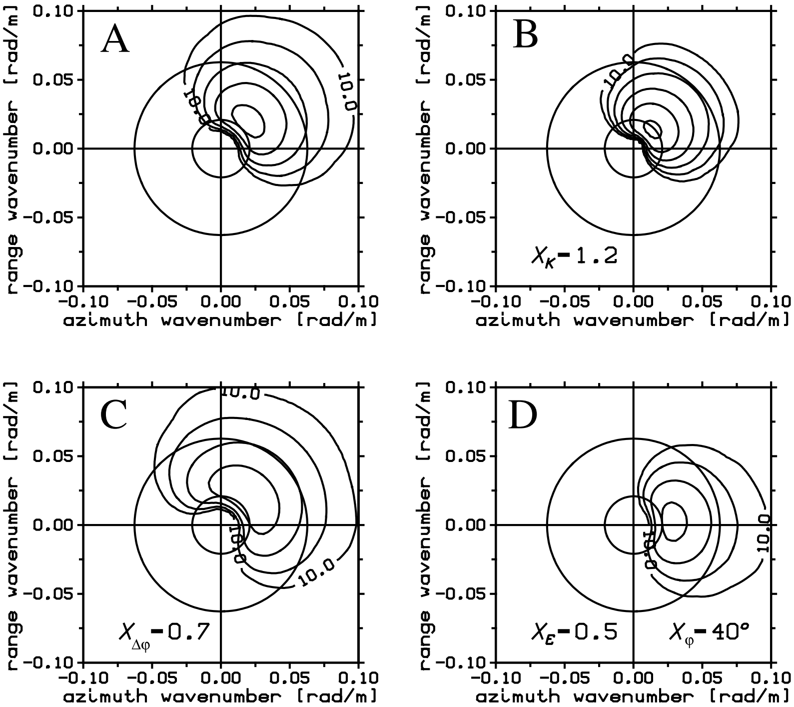

Figure 3. Transformations of wave systems used in the PARSA retrieval scheme (compare equation (12)). (a) Prior wave system with 250 m peak wavelength. Transformed wave spectra with (b) wave numbers rescaled, (c) directional spreading changed, and (d) simultaneous rotation and energy rescaling.

where the partition parameters $\hat{\mathbf{X}}^{\mathbf{i}}$ were collected into a vector $\overline{\mathbf{X}}$ of dimension 4 n_p:

$$\overline{\mathbf{X}} = \left(\hat{\mathbf{X}}^{\mathbf{1}}, \ldots, \hat{\mathbf{X}}^{n_p}\right). \tag{18}$$

The respective mean and standard deviation of $\overline{\mathbf{X}}$ are denoted by $\overline{\boldsymbol{\nu}}$ and $\overline{\boldsymbol{\sigma}}$. The statistical parameters used for the model describing errors in the prior model are summarized in Table 2. Again the given parameters are regarded as reasonable, however it is clear that the values strongly depend on the performance of the numerical model used to compute the prior wave spectrum, as well as the quality of the driving wind fields. It is obvious that any user of wave model data would benefit from knowledge about parameters like the ones used in this study and we think that it is simply a question of time until such information will be provided by weather centers on a routinely basis.

5. Numerical Inversion Procedure

[24] Inserting equations (8) and (17) in equation (2) and taking the logarithm we see that maximizing the conditional probability density function pdf($F_{\mathbf{k}}$, $\alpha|\Phi_{\mathbf{k}}$) is equivalent to minimizing the following cost function:

$$J(\mathbf{X}) = \sum_{\mathbf{k}\in\Pi} \frac{\left(\mathrm{Re}\left(\alpha_1\, e^{-k_x^2\,\beta^2\,\alpha_2}\,\Phi_{\mathbf{k}}^{\mathrm{sim}} - \Phi_{\mathbf{k}}^{\mathrm{obs}}\right)\right)^2}{\left(\sigma_{\mathbf{k}}^{\mathrm{Re}\Phi}\right)^2} + \frac{\left(\mathrm{Im}\left(\alpha_1\, e^{-k_x^2\,\beta^2\,\alpha_2}\,\Phi_{\mathbf{k}}^{\mathrm{sim}} - \Phi_{\mathbf{k}}^{\mathrm{obs}}\right)\right)^2}{\left(\sigma_{\mathbf{k}}^{\mathrm{Im}\Phi}\right)^2} + \sum_{i=1}^{4n_p+2} \frac{\left(\mathbf{X_i} - \mathbf{X_i^a}\right)^2}{\boldsymbol{\sigma}_i^2}, \tag{19}$$

where $\sigma_{\mathbf{k}}^{\mathrm{Re}\Phi}$ and $\sigma_{\mathbf{k}}^{\mathrm{Im}\Phi}$ are defined by

$$\left(\sigma_{\mathbf{k}}^{\mathrm{Re}\Phi}\right)^2 = \left(\sigma_{\mathbf{k}}^{RS}\right)^2 + \left(\sigma_{\mathbf{k}}^{\mathrm{RF}}\right)^2 \tag{20}$$

$$\left(\sigma_{\mathbf{k}}^{\mathrm{Im}\Phi}\right)^2 = \left(\sigma_{\mathbf{k}}^{IS}\right)^2 + \left(\sigma_{\mathbf{k}}^{\mathrm{IF}}\right)^2. \tag{21}$$

The transformation variables $\overline{\mathbf{X}}$ and $\boldsymbol{\alpha}$ were collected into the vector

$$\mathbf{X} = \left(\overline{\mathbf{X}}, \alpha_1, \alpha_2\right), \tag{22}$$

and mean and standard deviation are defined accordingly as

$$\mathbf{X^a} = (\overline{\boldsymbol{\nu}}, 1, 0) \quad \boldsymbol{\sigma} = (\overline{\boldsymbol{\sigma}}, \sigma_{\alpha_1}, \sigma_{\alpha_2}). \tag{23}$$

Equation (19) represents a nonlinear minimization problem with $N_X := 4\ n_p + 2$ variables, which is solved on the grid introduced in section 4.1.

5.1. Levenberg-Marquardt Method

[25] The inversion procedure is based on an iterative correction of the unknown vector $\mathbf{X}$,

$$\mathbf{X}^{(n+1)} = \mathbf{X}^{(n)} + \Delta\mathbf{X}, \tag{24}$$

Table 2. Standard Deviations of the Parameters Used for the Model Describing Errors in the Prior Wave Spectrum (Compare Equation (12))

σ_E	σ_k	σ_φ, deg	$\sigma_{\Delta\varphi}$
0.1	0.1	20	0.1

in each step replacing the nonlinear minimization problem equation (19) by a quadratic approximation, which is equivalent to a system of linear equations.

[26] The inversion is performed on a polar grid with $n_k \times n_\varphi/2 = 25 \times 18 = 450$ bins, which is an order of magnitude lower than the typical number of spectral bins of Cartesian grids (e.g., $128 \times 128 = 16384$) used by *Hasselmann et al.* [1996] or *Krogstad et al.* [1994]. The reduced dimension is an important feature of the proposed retrieval scheme as it becomes possible to include the coupling of different wave components in the imaging process in a numerical feasible way. It is thus possible to use an extension of the quasi-linear approximation of the SAR imaging model proposed by *Hasselmann and Hasselmann* [1991]. A disadvantage of that approach was the fact that the change of the cut-off factor resulting from a correction of the wave spectrum was not represented in the resulting quadratic problem. A way to deal with this shortcoming was later presented by *Hasselmann and Hasselmann* [1991] adding an explicit cut-off term in the cost function. In this study we try to avoid the problem right away by extending the quasi-linear approximation, such that the change of the azimuthal cutoff is explicitly contained. The following nondiagonal approximation of the Jacobian matrix is used to achieve this:

$$\frac{\partial \Phi_{\mathbf{k}}}{\partial F_{\mathbf{k}'}} \approx 0.5 \exp\left[-k_x^2 \beta^2 \rho^{uu}(\mathbf{0},0)\right] |T^S_{\mathbf{k}'}|^2 (\delta_{\mathbf{k}-\mathbf{k}'} \exp[i\omega_{\mathbf{k}}\Delta t] + \delta_{\mathbf{k}+\mathbf{k}'} \exp[-i\omega_{\mathbf{k}}\Delta t]) - \beta^2 k_x^2 |T^u_{\mathbf{k}'}|^2 \Phi_{\mathbf{k}}\, d\mathbf{k}. \tag{25}$$

Here, T^S and T^u are the SAR and orbital velocity transfer functions as defined in Appendix C. The approximation follows by applying the product rule to equation (C1) and approximating the derivative of the integral expression by the respective derivative at $F_{\mathbf{k}} = 0$.

[27] Denoting the correction of the vector $\mathbf{X}$ at the nth iteration step with $\Delta\mathbf{X}$ the resulting change ΔF^n of the wave spectrum $F_{\mathbf{k}}$ is given by

$$\Delta F^n_{\mathbf{k}} = \sum_{i=1}^{4n_p} \Delta \mathbf{X}_i \frac{\partial F_{\mathbf{k}}}{\partial \overline{\mathbf{X}}_i}. \tag{26}$$

The partial derivatives of the wave spectrum with respect to the parameter vector $\overline{\mathbf{X}}$ are estimated based on equation (12) using a bilinear interpolation method. For each wave spectrum $F^n_{\mathbf{k}}$ a simulated SLCS $\Phi^n_{\mathbf{k}}$ is calculated according to equation (C1). As the transform is defined on a Cartesian grid, the spectrum $F_{\mathbf{k}}$ is transformed accordingly using a bilinear interpolation method. The simulated SLCS $\Phi^{n+1}_{\mathbf{k}}$ of the next iteration step can then be written as

$$\Phi^{n+1}_{\mathbf{k}} \approx e^{-k_x^2\beta^2\alpha_2^n}\left(\alpha_1^n \Phi^n_{\mathbf{k}} + \alpha_1^n \sum_{\mathbf{k}'} \frac{\partial \Phi_{\mathbf{k}}}{\partial F_{\mathbf{k}'}} \Delta F^n_{\mathbf{k}'} + \Phi^n_{\mathbf{k}} \Delta\alpha_1 - \alpha_1^n k_x^2 \Phi^n_{\mathbf{k}} \Delta\alpha_2\right). \tag{27}$$

On the basis of the above approximations, the following cost function has to be minimized with respect to the unknown vector $\Delta\mathbf{X}$ in each iteration step:

$$\overline{J}(\Delta\mathbf{X}) = \left(\boldsymbol{\Phi}^{\mathrm{obs}} - \boldsymbol{\Phi}^n - D_n\,\Delta\mathbf{X}\right)^T S_\epsilon^{-1}\left(\boldsymbol{\Phi}^{\mathrm{obs}} - \boldsymbol{\Phi}^n - D_n\,\Delta\mathbf{X}\right) + (\Delta\mathbf{X} + \mathbf{X}^n - \mathbf{X}^{\mathbf{a}})^T S_a^{-1} (\Delta\mathbf{X} + \mathbf{X}^n - \mathbf{X}^{\mathbf{a}}). \tag{28}$$

Here we have switched to matrix notation for convenience. The Jacobian matrix D_n of dimension $2N \times N_X$ given by

$$D_n = \begin{pmatrix} \mathrm{Re}\, Z^1_{\mathbf{k}_1} & \cdots & \mathrm{Re}\, Z^{4n_p}_{\mathbf{k}_1} & \mathrm{Re} A_{\mathbf{k}_1} & \mathrm{Re} B_{\mathbf{k}_1} \\ \vdots & \vdots & \vdots & \vdots & \vdots \\ \mathrm{Re}\, Z^1_{\mathbf{k}_N} & \cdots & \mathrm{Re}\, Z^{4n_p}_{\mathbf{k}_N} & \mathrm{Re} A_{\mathbf{k}_N} & \mathrm{Re} B_{\mathbf{k}_N} \\ \mathrm{Im}\, Z^1_{\mathbf{k}_1} & \cdots & \mathrm{Im}\, Z^{4n_p}_{\mathbf{k}_1} & \mathrm{Im} A_{\mathbf{k}_1} & \mathrm{Im} B_{\mathbf{k}_1} \\ \vdots & \vdots & \vdots & \vdots & \vdots \\ \mathrm{Im}\, Z^1_{\mathbf{k}_N} & \cdots & \mathrm{Im}\, Z^{4n_p}_{\mathbf{k}_N} & \mathrm{Im} A_{\mathbf{k}_N} & \mathrm{Im} B_{\mathbf{k}_N} \end{pmatrix}, \tag{29}$$

with the wave number vectors $\mathbf{k}_1,\ldots, \mathbf{k}_N$ defined in equations (9) and (10). The complex valued functions $Z^i_{\mathbf{k}}$, $A_{\mathbf{k}}$, $B_{\mathbf{k}}$ are defined as

$$Z^i_{\mathbf{k}} = e^{-k_x^2\beta^2\alpha_2^n}\alpha_1^n \sum_{\mathbf{k}'} \frac{\partial \Phi_{\mathbf{k}}}{\partial F_{\mathbf{k}'}} \frac{\partial F_{\mathbf{k}'}}{\partial \overline{X}_i} \quad i = 1,..,4n_p, \tag{30}$$

$$A_{\mathbf{k}} = e^{-k_x^2\beta^2\alpha_2}\Phi^n_{\mathbf{k}}, \tag{31}$$

$$B_{\mathbf{k}} = -\alpha_1^n k_x^2 e^{-k_x^2\beta^2\alpha_2}\Phi^n_{\mathbf{k}}, \tag{32}$$

and the error covariance matrix S_ϵ of dimension $2N \times 2N$ is given by

$$S_\epsilon = \begin{pmatrix} \left(\sigma^{\mathrm{Re}\Phi}_{\mathbf{k}_1}\right)^2 & 0 & 0 & 0 & 0 & 0 \\ 0 & \ddots & 0 & 0 & 0 & 0 \\ 0 & 0 & \left(\sigma^{\mathrm{Re}\Phi}_{\mathbf{k}_N}\right)^2 & 0 & 0 & 0 \\ 0 & 0 & 0 & \left(\sigma^{\mathrm{Im}\Phi}_{\mathbf{k}_1}\right)^2 & 0 & 0 \\ 0 & 0 & 0 & 0 & \ddots & 0 \\ 0 & 0 & 0 & 0 & 0 & \left(\sigma^{\mathrm{Im}\Phi}_{\mathbf{k}_N}\right)^2 \end{pmatrix}. \tag{33}$$

Finally, the prior covariance matrix S_a of dimension $N_X \times N_X$ is defined as

$$S_a = \begin{pmatrix} (\boldsymbol{\sigma}_1)^2 & 0 & 0 \\ 0 & \ddots & 0 \\ 0 & 0 & (\boldsymbol{\sigma}_{4n_p+2})^2 \end{pmatrix}. \tag{34}$$

Table 3. General Parameters of the ERS-2 SAR Wave Mode

Parameter	Value
Radar frequency, GHz	5.300
Polarization	VV
Flight altitude, km	800
Velocity, km s^{-1}	7
Azimuth resolution, m	≈5
Slant range resolution, m	≈10
Look direction	right looking
Integration time Δt, s	0.66
Incidence angle θ, deg	23.5
β, s	111

Using the matrix notation equation (28) of the quadratic minimization problem, it can be shown [*Rodgers*, 2000] (compare Appendix B) that the next iterate $\mathbf{X}^{n+1}$ following from equation (24) can be written as

$$\begin{aligned}\mathbf{X}^{n+1} &= \mathbf{X}^n + C_X\left(D_n^T S_\epsilon^{-1}\left(\mathbf{\Phi}^{\text{obs}} - \mathbf{\Phi}^{\text{sim}}\right) - S_a^{-1}\left(\mathbf{X}^n - \mathbf{X}^a\right)\right) \\ &= \mathbf{X}^a + C_X D_n^T S_\epsilon^{-1}\left(\mathbf{\Phi}^{\text{obs}} - \mathbf{\Phi}^{\text{sim}} + D_n(\mathbf{X}^n - \mathbf{X}^a)\right), \end{aligned} \tag{35}$$

where C_X is the covariance matrix of $\mathbf{X}$ given by

$$C_X = \left(D_n^T S_\epsilon^{-1} D_n + S_a^{-1}\right)^{-1}. \tag{36}$$

To improve the convergence of the iteration scheme given by equation (35) in case of strong nonlinearities, a Levenberg- Marquardt approach is used. The idea is to blend the search direction given by the solution of the quadratic minimization problem, which might not reduce the cost function of the nonlinear problem in some cases, with the steepest gradient direction [*Rodgers*, 2000]. The resulting scheme is given by

$$\begin{aligned}\mathbf{X}^{n+1} &= \mathbf{X}^{\mathbf{a}} + \left(C_X^{-1} + \lambda^n I_{N_X}\right)^{-1} D_n^T S_\epsilon^{-1}(\mathbf{\Phi}^{\text{obs}} - \mathbf{\Phi}^{\text{sim}} \\ &\quad + D_n(\mathbf{X}^n - \mathbf{X}^a) + \lambda^n\left(\mathbf{X}^n - \mathbf{X}^{\mathbf{a}}\right)), \end{aligned} \tag{37}$$

where I_{N_X} is the identity matrix of dimension N_X and the parameter λ^n is adjusted during the iteration depending on the cost function values. In the PARSA scheme the following strategy was used:

$$\lambda^{n+1} = \begin{cases} 0.25\,\lambda^n & : \; J(\mathbf{X}^n) < J\left(\mathbf{X}^{n-1}\right) \\ 4\,\lambda^n & : \; J(\mathbf{X}^n) \geq J\left(\mathbf{X}^{n-1}\right) \end{cases}, \tag{38}$$

which results in an efficient iteration process.

5.2. Termination Criteria

[28] One important component of the numerical inversion scheme is the criterion used to terminate the iteration. For the PARSA scheme an approach proposed by *Rodgers* [2000] is used. A straightforward termination criterion follows from the natural requirement that the error should be an order of magnitude smaller than the variance of the wave spectra as given by the prior distribution. Because of the quadratic convergence of the inverse Hessian method this condition can be written as [*Rodgers*, 2000]

$$\left(\mathbf{X}^n - \mathbf{X}^{n-1}\right)^T C_X^{-1}\left(\mathbf{X}^n - \mathbf{X}^{n-1}\right) < T \ll N_X, \tag{39}$$

where C_X is the covariance matrix defined in equation (36) and $\mathbf{X}^n$, $\mathbf{X}^{n-1}$ are the parameter vectors in the current and previous iteration step respectively. The exact value for the termination threshold T is necessarily a compromise between accuracy and computational effort. For the retrievals shown in this study the value $T = N_X/15$ turned out to be a reasonable choice.

6. Test of Retrieval Using Simulated Data

[29] In a first step the PARSA scheme was tested using synthetic data, i.e., the observation was simulated from a known ocean wave spectrum. The same ocean wave spectrum was then transformed in different ways and used as a prior information for the retrieval. The ERS-2 SAR imaging parameters for wave mode as summarized in Table 3 are used for the tests. An important aspect of the retrieval performance is the ability of the scheme to reproduce the original wave spectrum. At the same time the scheme should avoid very strong corrections of the prior wave spectrum, which would lead to dynamical inconsistencies in a later assimilation of the retrieved spectra.

[30] Figure 4 shows a retrieval example with a single wind sea system. A parametric JONSWAP spectrum [*Hasselmann et al.*, 1980] was taken as a prior spectrum (lower right) assuming a fully developed sea state. The respective simulation of the real and imaginary part of the SLCS is shown on the bottom left. The observation to be used for the retrieval was simulated by transforming the prior spectrum with the parameters

$$\left(X_E, X_k, X_\varphi, X_{\Delta\varphi}\right) = (1.3, 1.1, 25^\circ, 1.2) \tag{40}$$

yielding the test spectrum F^{test} shown on the center right, and subsequent application of the full nonlinear SLCS transform (equation (C1)). The resulting real and imaginary parts of the observation are shown on the center left of Figure 4. Applying the PARSA scheme to the synthetic input data gave a retrieved wave spectrum F^{retr} (upper right) and imaging parameters α_1, α_2 after $N_{\text{iterate}} = 9$ iteration steps using the termination criteria described above. The respective simulated SLCS Φ^{retr} (upper left) was calculated using the retrieved wave spectrum as input to the transform equation (C1) and subsequent correction of the energy level and cut-off wavelength according to

$$\Phi^{\text{retr}} = \alpha_1 \exp\left[-k_x^2\,\beta^2\,\alpha_2\right]\Phi_{\mathbf{k}}^{\text{sim}}. \tag{41}$$

As one can see, the simulated SLCS Φ^{retr} shows almost perfect agreement with the observation Φ^{obs}. This is the case, although the parameters used to simulate the observation are not exactly reproduced as can be seen from the table given at the bottom of Figure 4. The small deviations become also visible comparing the retrieved wave spectrum F^{retr} with the test spectrum F^{test}. This behavior makes sense, because the PARSA scheme is designed such that it tries to explain deviations between the observed and simulated SLCS by both errors in the wave model and in the SAR imaging model. In the present case the scheme attributes the higher energy level of the observation to an underestimation of the integral transform

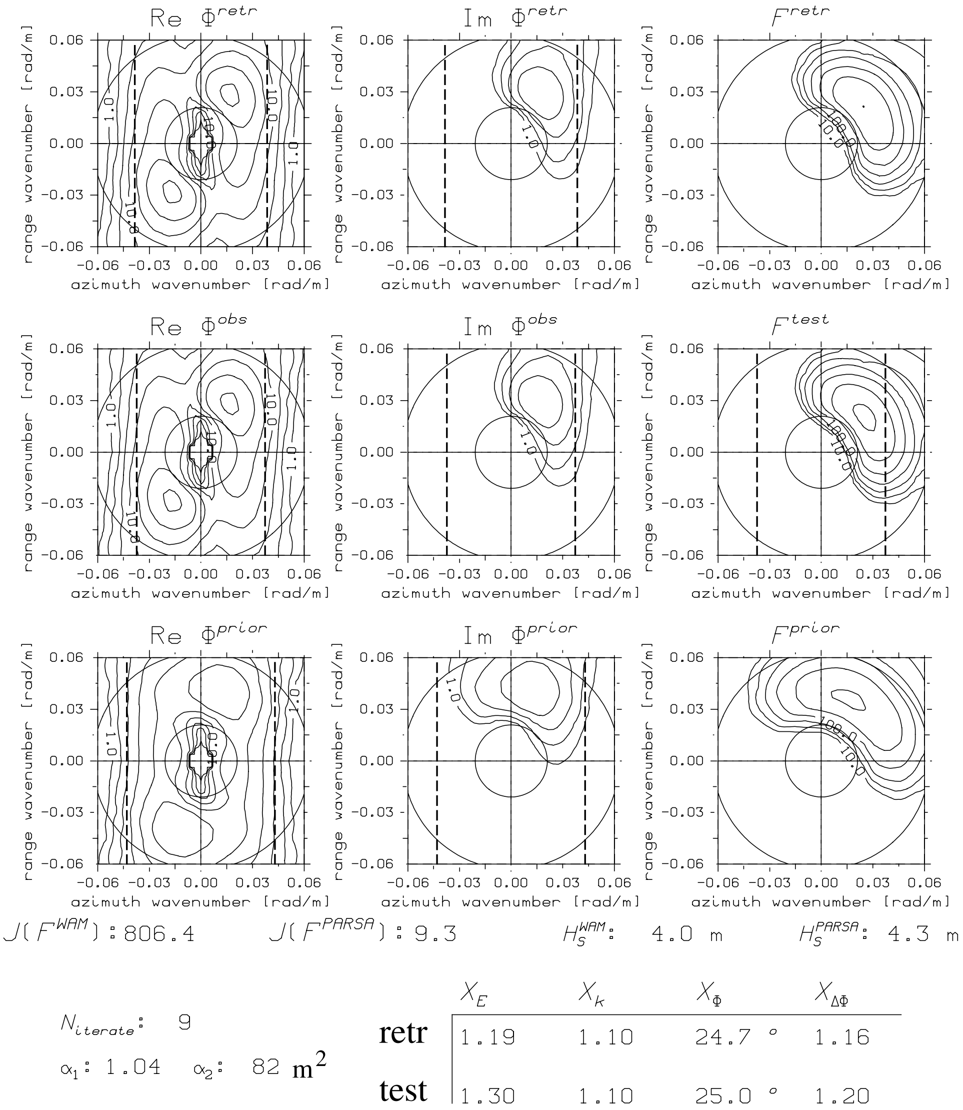

Figure 4. Retrieval example using simulated data with prior spectrum F^{prior} (bottom right), observed test synthetic aperture radar (SAR) look cross spectrum (SLCS) Φ^{obs} (center left), and retrieved wave spectrum F^{retr}. The SLCS Φ^{prior} and Φ^{retr} simulated from the prior wave spectrum and the retrieved spectrum are shown in the lower left and upper left, respectively. The spectrum F^{test} on the center right was used to simulate the observed SLCS (for details, see text).

(equation (C1)), represented by the parameter $\alpha_1 = 1.04$ and at the same time to an energy underestimation of the wave model represented by the parameter $X_E = 1.19$. Both the rotation parameter X_φ and the wave number rescaling parameter X_k are reproduced with good accuracy. Furthermore, the correction of the cut-off wavelength in the forward model is about 9 m and thus very small. The directional spreading parameter $X_{\Delta\varphi}$ is slightly lower than the prescribed value. Again this behavior makes sense, because the retrieval avoids any departure from the prior wave spectrum, which does not lead to an improved agreement between observed and simulated SLCS. As the agreement is already perfect with the lower value for $X_{\Delta\varphi}$, there is no reason for stronger corrections of the prior spectrum.

[31] The error statistics of the retrieval can be derived from the covariance matrix defined in equation (36). The following values were obtained for the standard deviations and correlations of the retrieved parameters for the present example:

$$\begin{pmatrix} \mathrm{stdv}X_E & \mathrm{cor}(X_E, X_k) & \mathrm{cor}(X_E, X_\varphi) & \mathrm{cor}(X_E, X_{\Delta\varphi}) \\ \cdot & \mathrm{stdv}X_k & \mathrm{cor}(X_k, X_\varphi) & \mathrm{cor}(X_k, X_{\Delta_\varphi}) \\ \cdot & \cdot & \mathrm{stdv}X_\varphi & \mathrm{cor}(X_\varphi, X_{\Delta_\varphi}) \\ \cdot & \cdot & \cdot & \mathrm{stdv}X_{\Delta\varphi} \end{pmatrix} = \begin{pmatrix} 0.05 & 0.3 & 0.7 & 0.3 \\ \cdot & 0.004 & 0.3 & -0.1 \\ \cdot & \cdot & 1.8^\circ & -0.1 \\ \cdot & \cdot & \cdot & 0.04 \end{pmatrix}.$$

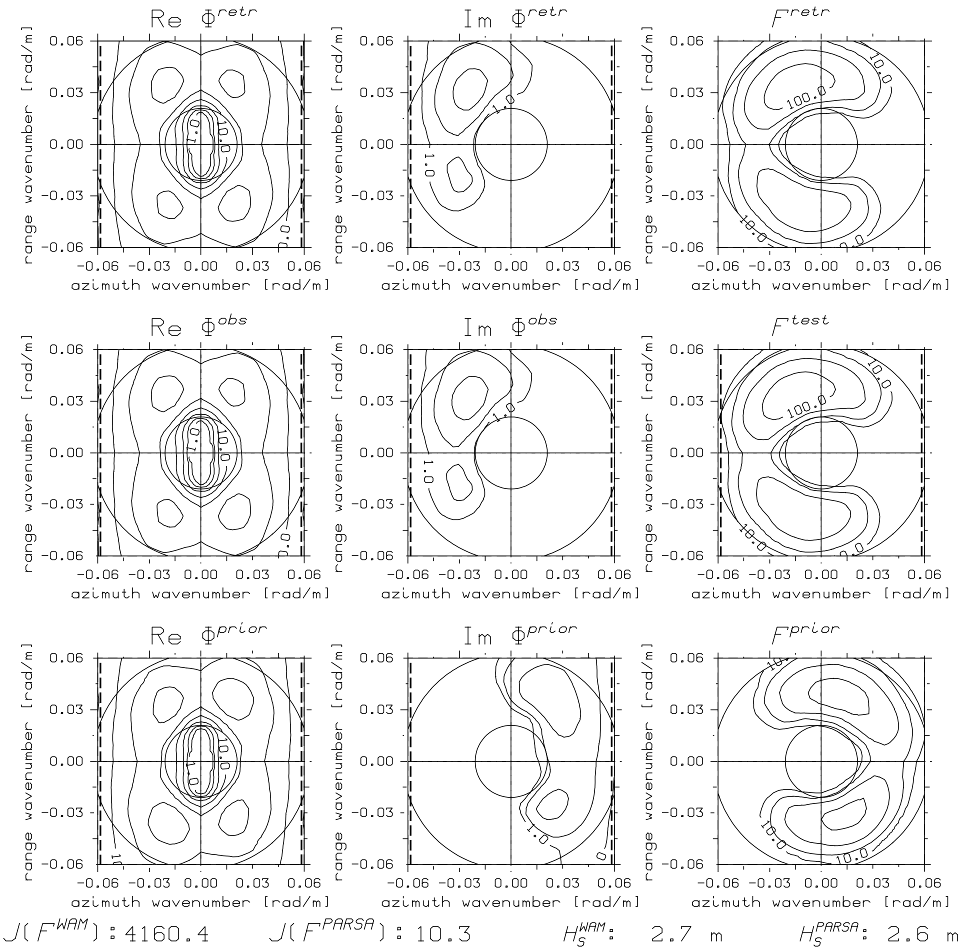

$N_{iterate}$: 14

α_1: 1.01 α_2: 12 m^2

		X_E	X_k	X_Φ	$X_{\Delta\Phi}$
retr	1st	1.07	1.03	−38.9°	1.02
	2nd	0.90	0.97	39.6 °	0.99
test	1st	1.10	1.03	−40.0°	1.00
	2nd	0.90	0.97	40.0 °	1.00

Figure 5. Retrieval example using simulated data with prior spectrum F^{prior} (bottom right), observed test SLCS Φ^{obs} (center left), and retrieved wave spectrum F^{retr}. The SLCS Φ^{prior} and Φ^{retr} simulated from the prior wave spectrum and the retrieved spectrum are shown in the lower left and upper left, respectively. The spectrum F^{test} on the center right was used to simulate the observed SLCS (for details, see text).

In particular, one can see that the standard deviations of the retrieved parameters are smaller than the respective values of the prior distribution (compare Table 2). This means that despite the significant errors assumed in the SLCS estimation and the imaging model, the SAR measurement does add information to the knowledge already provided by the ocean wave model.

[32] Another retrieval example based on synthetic data, which is supposed to demonstrate the benefit of the additional complex information represented by the imaginary part of the SLCS is shown in Figure 5. As one can see, the prior spectrum contains two wave systems with almost opposite propagation directions in this case. As in the first example an observation was generated by simulation. In this case the following parameters were used to transform the spectrum:

$$\left(X_E^1, X_k^1, X_\varphi^1, X_{\Delta\varphi}^1, X_E^2, X_k^2, X_\varphi^2, X_{\Delta\varphi}^2\right) = (1.1, 1.03, -40^\circ, 1, 0.9, 0.97, 40^\circ, 1). \tag{42}$$

Here, the first index refers to the wave system at the top and the second index to the wave system at the bottom. The SLCS Φ^{prior} simulated from the prior wave spectrum shows good agreement with the observation in the real part, however strong deviations are found in the imaginary part. It is clear, that if there was no complex information available as in the case of conventional variance spectra,

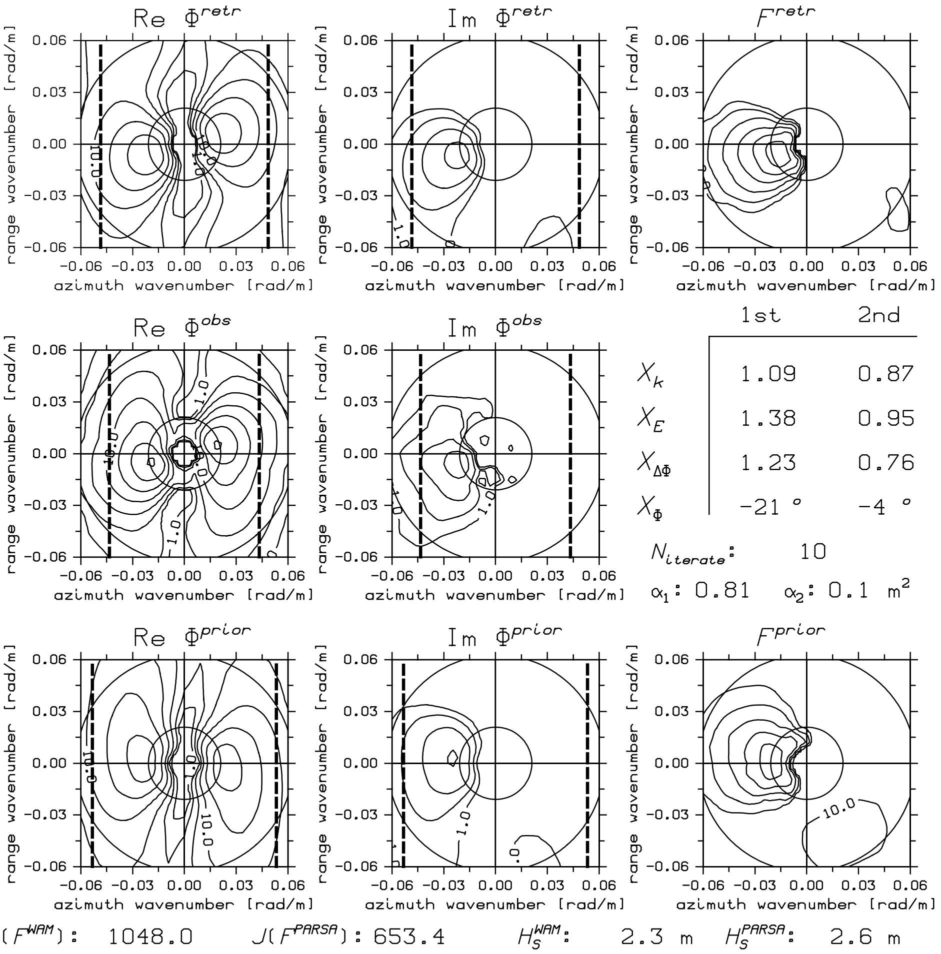

Figure 6. PARSA retrieval for an ERS-2 SLCS acquired in the Indian Ocean at 23.46°S 64.36°E on 5 September 1996, 0546 UTC. The satellite heading is 192.94°. The dashed vertical lines indicate the azimuthal cut-off wavelength.

there would be no reason to modify the prior wave spectrum apart from small changes of energy and wavelength. However, the retrieved spectrum calculated with the PARSA scheme within N_{iterate} = 14 iteration steps shows that the information in the imaginary part helps to apply more significant corrections, rotating both wave systems correctly by almost 40°. The inversion example demonstrates that, although the overall shape of the wave spectrum is taken from the wave model and thus most ambiguities in wave propagation direction are resolved by prior knowledge, the imaginary part adds valuable information in multisystem cases.

7. Application to Reprocessed ERS-2 Data

[33] In a second step, the retrieval scheme was applied to a global data set of 11000 reprocessed ERS-2 wave mode imagettes introduced by *Lehner et al.* [2000]. SLCS given on the same polar grid as used for the ENVISAT wave mode product were processed from the ERS-2 data and used as input for the PARSA scheme. Two-dimensional wave model spectra provided by the ECMWF were used a prior information. The data are standard output from the operational WAM model runs performed at ECMWF at the four synoptical hours 0000, 0600, 1200, and 1800 UTC. The temporal gap between WAM and SAR measurement is thus less than 3 hours. The model is driven by U_{10} wind fields computed with the atmospheric general circulation model (AGCM). The operational WAM model was run on a 1.5° × 1.5° latitude-longitude grid. The collocation distance to the ERS-2 imagettes is thus less than 0.75°.

7.1. Case Studies

[34] Figures 6–7 show two inversion examples calculated with the PARSA scheme. The first case presented in Figure 6 is a swell dominated situation in the Indian Ocean with a wave system of about 300 m wavelength propagating in the negative azimuth direction (to the left) and an old wind sea system of about 150 m wavelength in the negative range direction (downward). The wind speed according to the ECMWF model was 3.2 ms^{-1} explaining the relatively short cut-off wavelength of about 135 m in the observed SLCS. The PARSA scheme retrieved the wave spectrum shown on the upper right within 12 iteration steps reducing the cost function value by about 40%. It can be clearly seen that the retrieval scheme improves the agreement between

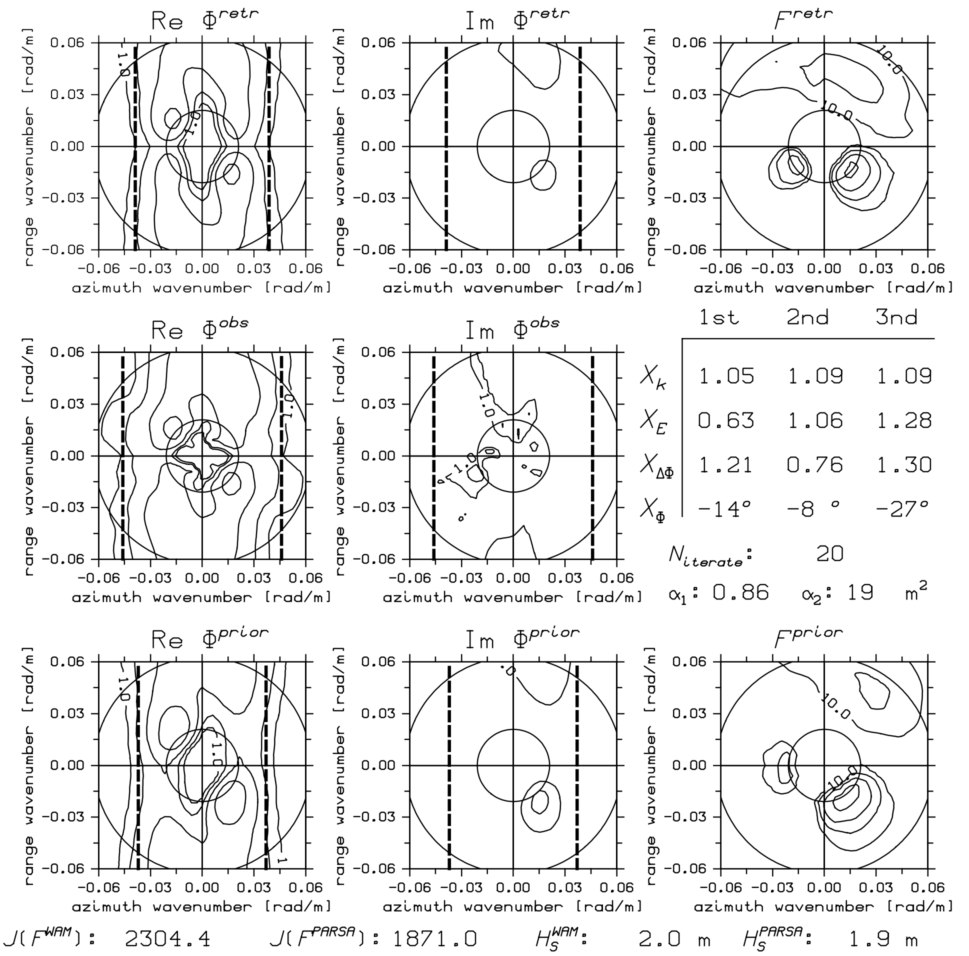

Figure 7. PARSA retrieval for an ERS-2 SLCS acquired in the Pacific at 12.46°S 139.45°W on 5 September 1996, 0806 UTC. The heading of the satellite is 347°.

the simulated and the observed SLCS including the azimuthal cut-off wavelength. This is mainly achieved by rotating the swell system by about 21° in the anticlockwise direction. At the same time, the directional spreading is reduced and the wavelength increased to about 330 m. The energy of the swell system is increased by 38%. One can see that the second system is turned in the azimuth direction, scaled down in energy and reduced in wavelength. The rescaling of the two wave system results in a slight increase of the significant wave height from 2.3 m to 2.6 m.

[35] The second retrieval shown in Figure 7 is an example for a more complicated situation in the Pacific with two swell systems of about 300 m wavelength coming from the south (left system) and the north east (lower right system) and an additional wind sea system with about 150 m wavelength. The PARSA retrieves a wave spectrum after 28 iterations reducing the cost function by about 20%. Again the agreement between simulated and observed SLCS is significantly improved by the retrieval. It is interesting to note in this case that the swell system propagating to the left is not visible in the observed real part of the SLCS, but shows up in the respective imaginary part. As can be seen this information is taken from the PARSA scheme and used to rotate the prior system in anticlockwise direction. The example is thus another demonstration, that the complex information provided by the SLCS is actually used in the retrieval.

7.2. Statistical Analysis

[36] Figure 8 shows some general statistics about the data set with the distribution of the number of partitions given in Figure 8a. One can see that about half of the WAM spectra contain two partitions and for the remaining cases the spectra with one partition and three partitions have about equal share. Figure 8b gives the respective distribution of the maximum energies observed in the SLCS. The vertical line gives a rough estimate of the expected noise level in the SLCS as a reference. For details on SLCS noise see *Schulz-Stellenfleth and Lehner* [2005]. One can see that the histogram has a maximum at a signal to noise ratio (SNR) of roughly 5 dB. About 20% of the cases have a SNR of 10 dB or more.

[37] Figure 9 gives some general statistics about the performance of the inversion scheme. The distribution of the number of iterations is depicted in Figure 9a. One can see that the majority of cases requires less than 10 iterations. The achieved reduction of the cost function is illustrated in Figure 9b, where the distribution of the ratio of the first and

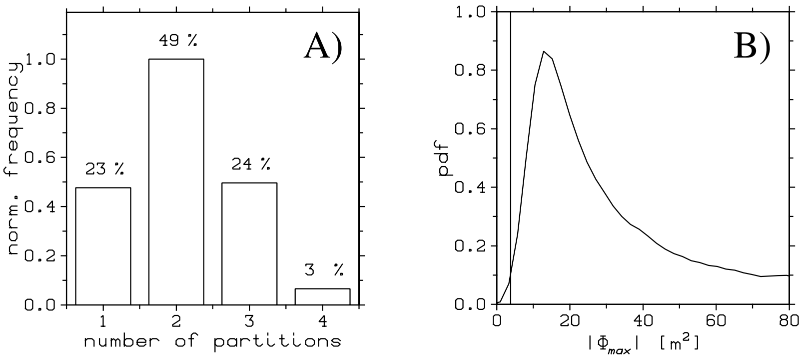

Figure 8. (a) Distribution of the number of partitions in a global data set of 11,000 WAM wave spectra. (b) Distribution of the maximum magnitude of the respective ERS-2 SLCS.

final cost function value is shown. One can see that in about half of the cases the inversion scheme reduces the cost function by more than 20%.

[38] A statistical comparison of prior wave spectra and retrieved spectra was carried out in terms of the significant wave height H_s. Furthermore, the mean frequency $\overline{f}$, defined as

$$\overline{f} = \frac{1}{16\,H_s^2} \int df\; d\varphi\, f\; F_{f,\varphi}, \tag{43}$$

and the mean direction $\overline{\varphi}$, given by

$$\overline{\varphi} = \arctan\left(\frac{\int dfd\varphi\;\sin\varphi\; F_{f,\varphi}}{\int dfd\varphi\;\cos\varphi\; F_{f,\varphi}}\right), \tag{44}$$

were analyzed. Here $F_{f,\varphi}$ is the directional frequency spectrum, which is related to the wave number spectrum $F_{\mathbf{k}}$ via equation (11).

[39] Figure 10 shows a global map with mean directions and wave heights derived from ECMWF spectra (black arrows) and corresponding PARSA retrievals (red arrows) for ERS-2 wave mode data acquired on 5 September 1996. One can see that although the general agreement is good, differences in wave height and direction occur in particular in the areas of high sea states on the Southern hemisphere. For instance, there is a tendency of the retrieval to slightly increase the wave height at high sea states. This observation is consistent with earlier studies [*Bentamy et al.*, 1996], which suggest that the model wind speeds on the southern hemisphere are too weak in many cases. It is also interesting to note that the observed corrections of the mean direction look reasonable in the way that the rotations are changing smoothly going from one imagette to the next one along the track. This observation gives some confidence that the corrections are in fact due to large-scale errors in the driving wind field. A good example is the North Atlantic where waves of up to 5 m height are seen propagating in easterly direction. These waves were generated by a cyclone, which propagated along the North American east coast (Edward). It can be seen that the retrieval scheme rotates the mean direction in the clockwise direction over a distance of about 1500 km. It can also be seen that the rotation is not always toward the range axis of the sensor as one might suspect due to the velocity bunching effect.

[40] The general findings visible on the global map can be confirmed looking at the respective scatter plots shown in Figure 11. The plots are based on 11000 retrievals, with SAR data acquired in August/September 1996, i.e., in late Australian winter, with strong storms in the southern Atlantic, Pacific and Indian Oceans and a couple of hurricanes in the North Atlantic.

[41] First of all, one can see that the agreement of model wave height and retrieved wave height shown in Figure 11a is very good with a correlation of 0.93 and a rms of 0.51 m.

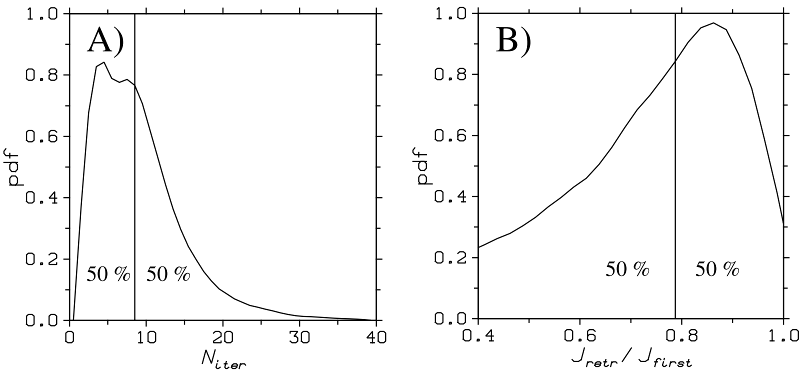

Figure 9. (a) Histogram of the number of iteration steps required in the PARSA retrieval estimated from 11,000 inversions. (b) Histogram of the relative cost function reduction achieved by the PARSA scheme.

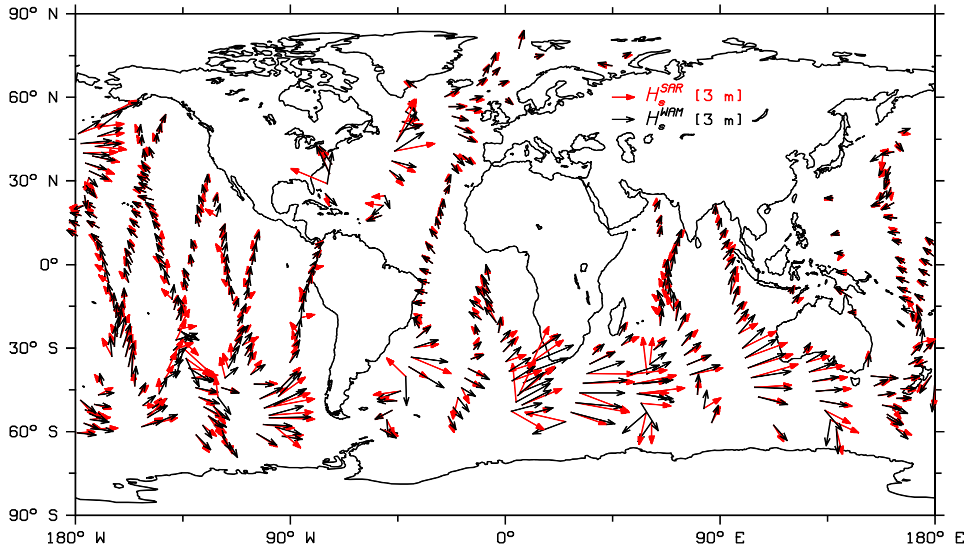

Figure 10. Comparison of significant wave height and mean direction of two-dimensional wave spectra computed with the WAM model (black) and respective PARSA retrievals (red) using ERS-2 SLCS acquired on 5 September 1996.

This high correlation has two main reasons: (1) due to the fact that strong errors in the energy level of the simulated SLCS are assumed (compare equation (6)) the retrieval takes a lot of wave height information from the model and (2) only cases which failed the inhomogeneity test described by *Schulz-Stellenfleth and Lehner* [2005] were disregarded as input for the retrieval, i.e., the data set contains a significant number of spectra with very low SNRs, in which case the inversion scheme tends to stay close to the prior spectrum. However, one can see that despite the lack of trust in the simulated energy levels the PARSA scheme still indicates an underprediction of wave heights at high sea states in the order of 30 cm for wave heights above 8 m. As pointed out above, this observation is consistent with earlier studies suggesting that the driving model wind fields in the "rolling fourties" and "fighting fifties" are a bit too low.

[42] The comparison of the mean frequencies in the model and the retrieval shown in Figure 11c indicates an underprediction of wavelength in the wave model. This observation again makes sense taking into account that the wave height underprediction for the high wind seas discussed above is consistent with a wavelength underprediction.

[43] The comparison of mean directions shown in Figure 12a exhibits a homogeneous behavior, i.e., there are no pronounced imaging artefacts or asymmetries visible. Figure 12b shows the directional spread parameter $X_{\Delta\varphi}$ depending on wave frequency. The plot shows a symmetric scatter of the parameter around its mean with stronger deviations for longer waves.

[44] One has to point out that the scatterplots discussed above do not represent validations of any kind. They just show in which direction the SAR observations are "pulling" the numerical model.

[45] Figure 13 shows a scatterplot of the parameters α_1, α_2 describing errors in the SAR imaging model, which are estimated as part of the PARSA retrieval process. One can

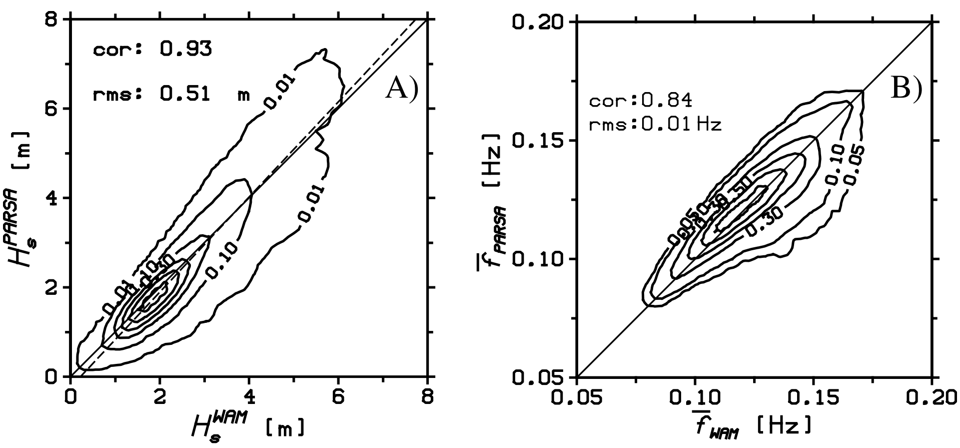

Figure 11. Comparison of (a) significant wave height and (b) mean frequency of WAM model spectra and respective PARSA retrievals.

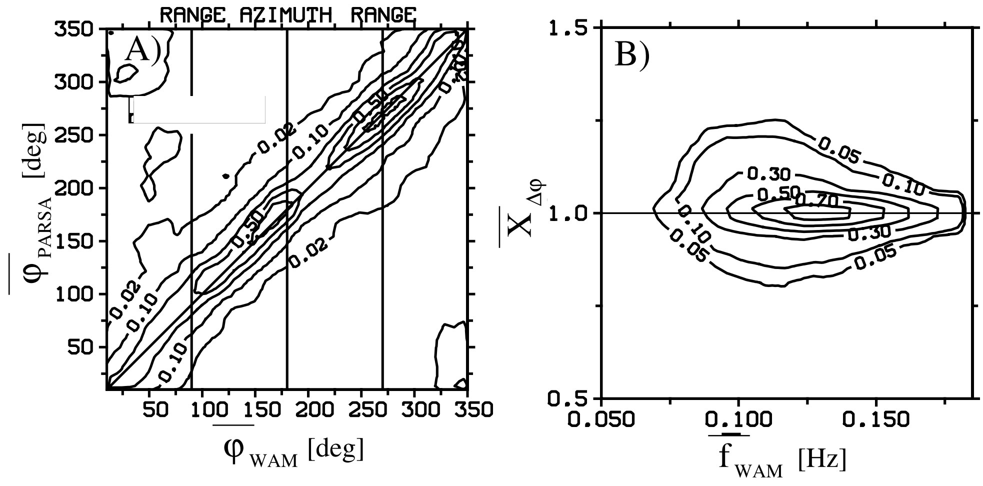

Figure 12. (a) Comparison of mean wave direction (compare equation (44)) in WAM model spectra and the respective PARSA retrievals. (b) Distribution of the directional spread parameter $X_{\Delta\varphi}$ (compare equation (12)) depending on frequency.

see that both parameters are slightly shifted above the mean of their prior distribution. For α_1 the retrievals indicate that the energy level of the theoretical forward model is about 10% too low. The respective finding for α_2 shows that the azimuthal cut-off wavelengths in the imaging model are slightly too short.

8. Conclusions

[46] A new retrieval scheme for the estimation of 2-D ocean wave spectra from SLCS and prior wave model spectra was presented. The study represents the first rigorous theoretical and statistical analysis of the subject and is believed to be an important step toward an efficient use of SLCS in operational forecast systems.

[47] The PARSA scheme is based on explicit models for uncertainties in the SAR imaging model as well as errors in the SAR observation and the wave model spectra used as prior information. The approach in particular enables the estimation of the error covariance matrix of the retrieved parameters. The scheme provides estimates of uncertain parameters in the SAR imaging model as additional retrieval results. Furthermore a new wave spectra partitioning technique was introduced, which allows overlapping wave systems to avoid discontinuities in the retrieved spectra.

[48] It was shown that the retrieval scheme is able to improve the agreement of simulated and observed SLCS efficiently. Furthermore it was demonstrated that the scheme makes explicit use of the complex information in the SLCS. This in particular shows that SLCS are preferable to the symmetric SAR image variance spectra used so far.

[49] The performance of the scheme was analyzed using both simulated and measured SAR data. The global analysis was based on a data set of 11000 ERS-2 SLCS and colocated WAM spectra provided by the ECMWF. It was shown that the inversion scheme requires less than 10 iterations in most of the cases. In about half of the cases the inversion reduces the cost function by more than 20%. A comparison of retrieved spectra and prior spectra was performed in terms of significant wave height, mean frequency and mean direction based on scatterplots and global maps. It is important to note that this comparison is not a validation of the scheme, which has to be done using additional in situ data. The statistics indicated a slight overestimation of the mean wave frequency in the numerical wave model. A slight underestimation of the model wave height was found for high sea states. At the same time the inversions suggest that the modulus of the SLCS simulated with the theoretical SAR imaging model is slightly too low and the respective azimuthal cut-off wavelength too short.

[50] The scheme is currently tested using a collocated data set of buoys and ENVISAT SLCS, which were collected in the framework of the ENVISAT calibration and validation activities. The respective comparisons will

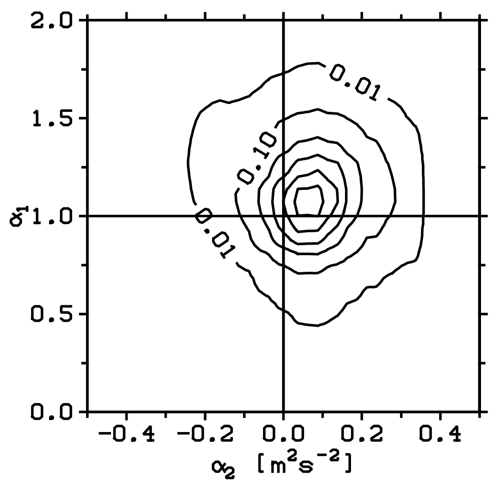

Figure 13. Scatterplot of the parameters α_1, α_2 in the error model of the SAR imaging model (compare equation (6)).

in particular be used to fine tune the SAR imaging model.

Appendix A: Wave Spectra Partitioning

[51] The partitioning method used in the PARSA scheme avoids discontinuities, which can occur in the scheme proposed by *Gerling* [1992] in cases where partitions are close together. The main difference is that spectral regimes of different partitions can overlap in the new scheme, whereas the partitions by *Gerling* [1992] are completely distinct.

[52] The method starts with the determination of the local maxima in the wave spectrum. Lets denote the location of the local maxima on the polar grid with ($k^1_{\max}$, $\varphi^1_{\max}$),. . ., ($k^{n_p}_{\max}$, $\varphi^{n_p}_{\max}$) and the respective spectral energies with $F^{(1)}_{\max}$, . . ., $F^{(n_p)}_{\max}$. For all local maxima respective partitions $B^{(1)}_{\mathbf{k}}$,. . ., $B^{(n_p)}_{\mathbf{k}}$ are defined, which have to fulfil

$$\sum_{i=1}^{n_p} B^{(i)}_{\mathbf{k}} = F_{\mathbf{k}}. \tag{A1}$$

The partitions $B^{(i)}_{\mathbf{k}}$ are chosen such that the energy ratio in each grid point reflects the distance $d^{(i)}_{\mathbf{k}}$ to the respective local maxima, i.e., the energy contribution of a partition far away from a certain grid point should be smaller than the respective contribution of a closer partition. At the same time the ratio also has to reflect the energy levels of the different partitions as indicated by the respective maxima. A simple approach to achieve this is to impose the following conditions:

$$B^{(1)}_{\mathbf{k}} \frac{d^{(1)}_{\mathbf{k}}}{F^{(1)}_{\max}} = B^{(2)}_{\mathbf{k}} \frac{d^{(2)}_{\mathbf{k}}}{F^{(2)}_{\max}} = \ldots = B^{(n_p)}_{\mathbf{k}} \frac{d^{(n_p)}_{\mathbf{k}}}{F^{(n_p)}_{\max}}, \tag{A2}$$

where $d_{\mathbf{k}}$ is some distance measure, which was chosen a

$$d^{(i)}_{\mathbf{k}} = \frac{\left(k^i_{\max} - k\right)^4}{\left(\Delta k^i\right)^4} + \frac{\left(\varphi - \varphi^i_{\max}\right)^4}{\left(\Delta\varphi^i\right)^4} \tag{A3}$$

with 3dB width of the partition given by Δk^i and $\Delta\varphi^i$. The distance measure equation (A3) is an ad hoc formulation, which turned out to give a good separation and smooth boundaries of the partitions for the investigated cases. Nevertheless an approach with a stronger physical foundation is desirable and will be developed in future versions. Equations (A1) and (A2) represent a linear system of n_p equations, which can be solved for each grid point yielding the partitions $B^{(i)}_{\mathbf{k}}$, $i = 1,\ldots, n_p$. If $\mathbf{k}$ does not happen to be one the local maxima the partitions can be written as follows:

$$B^{(j)}_{\mathbf{k}} = F_{\mathbf{k}} \frac{F^{(j)}_{\max}}{d^{(j)}_{\mathbf{k}}} \left(\sum_{i=1}^{n_p} \frac{F^{(i)}_{\max}}{d^{(i)}_{\mathbf{k}}} \right)^{-1}. \tag{A4}$$

If $\mathbf{k}$ coincides with one of the local maxima all partitions are zero except for the one associated with that maximum.

Appendix B: Posterior Distribution in the Linear Case

[53] Let $\mathbf{X}$ be a Gaussian distributed state vector with mean $\mathbf{X^a}$ and covariance matrix S_a. Furthermore, a Gaussian distributed measurement vector $\mathbf{Y}$ is given, which has zero mean and covariance matrix S_ϵ. If furthermore the forward model, describing the mapping of a state vector into the respective measurement space, is linear with Jacobian matrix D, the conditional probability of the state vector $\mathbf{X}$ given the measurement $\mathbf{Y}$ can be written as [*Rodgers*, 2000]

$$\mathrm{pdf}(\mathbf{X}|\mathbf{Y}) \sim \exp\left[-\frac{1}{2}(\mathbf{X} - \hat{\mathbf{X}})^T C_X^{-1} (\mathbf{X} - \hat{\mathbf{X}})\right], \tag{B1}$$

with covariance matrix C_X given by

$$C_X = \left(D^T S_\epsilon^{-1} D + S_a^{-1}\right)^{-1} \tag{B2}$$

and mean state vector calculated as

$$\hat{\mathbf{X}} = C_X \left(D^T S_\epsilon^{-1} \mathbf{Y} + S_a^{-1} \mathbf{X^a}\right). \tag{B3}$$

The expression in equation (B1) is referred to as posterior pdf.

Appendix C: Integral SAR Transform for SLCS

[54] The following integral transform relates the 2-D wave spectrum $F_{\mathbf{k}}$ to the SLCS of the normalized looks $I^i = \langle I_\sigma \rangle^{-1} (I^i_\sigma - \langle I_\sigma \rangle)$, i = 1, 2 separated by the time Δt [*Engen and Johnsen*, 1995]:

$$\begin{aligned} \Phi^{I^1 I^2}_{\mathbf{k}} = {} & \frac{1}{4\,\pi^2} \exp\left[-k_x^2 \beta^2\, \rho^{uu}(\mathbf{0}, 0)\right] \int d^2x \exp[-i\,\mathbf{k}\,\mathbf{x}] \\ & \cdot \exp\left[k_x^2\, \beta^2\, \rho^{uu}(\mathbf{x}, \Delta t)\right] \left[1 + \rho^{RR}(\mathbf{x}, \Delta t) + i\, k_x \beta \left(\rho^{Ru}\mathbf{x}, \Delta t\right)\right. \\ & - \rho^{Ru}(-\mathbf{x}, -\Delta t)) + (k_x\, \beta)^2 \left(\rho^{Ru}(\mathbf{x}, \Delta t) - \rho^{Ru}(\mathbf{0}, 0)\right) \\ & \left. \cdot \left(\rho^{Ru}(-\mathbf{x}, -\Delta t) - \rho^{Ru}(\mathbf{0}, 0)\right)\right], \end{aligned} \tag{C1}$$

with cross- and auto-covariance functions ρ^{RR}, ρ^{uu} and ρ^{Ru} defined according to

$$\begin{aligned} \rho^{XY}(\mathbf{x}, \Delta t) = 0.5 \int & d^2k \left(F_{\mathbf{k}}\, T^X_{\mathbf{k}} \left(T^Y_{\mathbf{k}}\right)^* \exp[i\,\omega_{\mathbf{k}}\,\Delta t]\right. \\ & \left. + F_{-\mathbf{k}} \left(T^X_{-\mathbf{k}}\right)^* T^Y_{-\mathbf{k}} \exp[-i\,\omega_{\mathbf{k}}\,\Delta t]\right) \exp[i\,\mathbf{k}\,\mathbf{x}]. \end{aligned} \tag{C2}$$

Here, β is the ratio of slant range and platform velocity (compare Table 3). The transfer function T^R is given by

$$T^R_{\mathbf{k}} = T^{\mathrm{tilt}}_{\mathbf{k}} + T^{\mathrm{hydr}}_{\mathbf{k}} + T^{rb}_{\mathbf{k}}, \tag{C3}$$

where T^{tilt} represents tilt modulation, T^{hydr} hydrodynamic modulation, and T^{rb} range bunching [*Hasselmann and Hasselmann*, 1991]. For vertical polarization in transmit and receive (VV) and a right looking SAR, analytical expressions for the transfer functions are given by

$$T^{\mathrm{tilt}}_{\mathbf{k}} = -\frac{4\, i\, k_y \cot\theta}{1 + \sin^2\theta}, \tag{C4}$$

$$T^{rb}_{\mathbf{k}} = -i\, k_y \frac{\cos\theta}{\sin\theta}, \tag{C5}$$

$$T_{\mathbf{k}}^{\mathrm{hydr}} = 4.5\,\omega_{\mathbf{k}}\,\frac{k_y^2}{|k|}\,\frac{\omega_{\mathbf{k}} - i\mu}{\omega_{\mathbf{k}}^2 + \mu^2}. \tag{C6}$$

Here, θ is the incidence angle (compare Table 3) and μ is the hydrodynamic relaxation rate which was set to 0.5 s^{-1} in the open water [*Hasselmann and Hasselmann*, 1991]. The k_x and k_y components refer to a right handed coordinate system with k_x pointing in flight direction. The orbital velocity transfer function is given by

$$T_{\mathbf{k}}^{u} = -\omega_{\mathbf{k}}\left(\frac{k_y}{|k|}\,\sin\theta + i\,\cos\theta\right). \tag{C7}$$

A linear and quasi-linear approximation of the SAR imaging mechanism can, e.g., be found by *Hasselmann and Hasselmann* [1991].

[55] **Acknowledgments.** The present study was sponsored by the German Ministry of Education, Science and Technology (BMBF) in the framework of the ENVOC project. We would like to thank the European Space Agency (ESA) for providing ERS-2 wave mode raw data in the framework of the ERS-AO3 project COMPLEX (ID 999192). Furthermore, we thank the reviewers for their careful reading of the manuscript.

References

Alpers, W. R., D. B. Ross, and C. L. Rufenach (1981), On the detectability of ocean surface waves by real and synthetic aperture radar, *J. Geophys. Res.*, *86*, 6481–6498.

Bentamy, A., N. Grima, Y. Quilfen, V. Harscoat, C. Maroni, and S. Pouliquen (1996), An atlas of surface wind from ERS-2 scatterometer measurements 1991–1996, technical report, Fr. Res. Inst. for Exploitation of the Sea, Issy-les-Moulineaux, France.

Breivik, L.-A., M. Reistad, H. Schyberg, J. Sunde, H. E. Krogstad, and H. Johnsen (1998), Assimilation of ERS SAR wave spectra in an operational wave model, *J. Geophys. Res.*, *103*, 7887–7900.

Brüning, C., R. Schmidt, and W. Alpers (1994), Estimation of the ocean wave-radar modulation transfer function from synthetic aperture radar imagery, *J. Geophys. Res.*, *99*, 9803–9815.

Chapron, B., H. Johnsen, and R. Garello (2001), Wave and wind retrieval from SAR images of the ocean, *Ann. Telecommun.*, *56*, 682–699.

Dowd, M., and P. W. Vachon (2001), Ocean wave extraction from RADARSAT Synthetic Aperture Radar Inter-Look Image Cross Spectra, *IEEE TGARS*, *39*, 21–37.

Engen, G., and H. Johnsen (1995), SAR-ocean wave inversion using image cross spectra, *IEEE Trans. Geosci. Remote Sens.*, *33*, 1047–1056.

Engen, G., H. Johnsen, K. Høgda, and B. Chapron (2001), ENVISAT ASAR Level 2 wave mode product algorithm specification—Software requirement document, *Tech. Rep. NORUT IT 650/1-01*, vers. 2.2.5, Oct., Norut IT, Tromsø, Norway.

Gerling, T. W. (1992), Partitioning sequences and arrays of directional ocean wave spectra into component wave systems, *J. Athmos. Oceanic Technol.*, *9*, 444–458.

Hasselmann, D. E., M. Dunckel, and J. A. Ewing (1980), Directional wave spectra observed during JONSWAP 1973, *J. Phys. Oceanogr.*, *10*, 1264–1280.

Hasselmann, K., and S. A. Hasselmann (1991), On the nonlinear mapping of an ocean wave spectrum into a synthetic aperture radar image spectrum and its inversion, *J. Geophys. Res.*, *96*, 10,713–10,729.

Hasselmann, S., C. Brüning, K. Hasselmann, and P. Heimbach (1996), An improved algorithm for the retrieval of ocean wave spectra from synthetic aperture radar image spectra, *J. Geophys. Res.*, *101*, 16,615–16,629.

Heimbach, P., S. Hasselmann, and K. Hasselmann (1998), Statistical analysis and intercomparison of WAM model data with global ERS-1 SAR wave mode spectral retrievals over 3 years, *J. Geophys. Res.*, *103*, 7931–7977.

Honerkamp, J. (1993), *Stochastic Dynamical Systems*, VCH Verlagsgesellschaft mbH, New York.

Johnsen, H., G. Engen, B. Chapron, N. Walker, and Y.-L. Desnos (2002), The ASAR wave mode: Level 1 and 2 algorithms and products, in *Proceedings of the ENVISAT Calibration Review* [CD-ROM], paper asar_21, Eur. Space Agency, Noordwijk, Netherlands.

Krogstad, H., O. Samset, and P. W. Vachon (1994), Generalizations of the nonlinear ocean-SAR transformation and a simplified SAR inversion algorithm, *Atmos. Ocean*, *32*, 61–82.

Lehner, S., J. Schulz-Stellenfleth, B. Schättler, H. Breit, and J. Horstmann (2000), Wind and wave measurements using complex ERS-2 SAR wave mode data, *IEEE TGARS*, *38*, 2246–2257.

Lyzenga, D. R. (1986), Numerical simulation of synthetic aperture radar image spectra for ocean waves, *IEEE Trans. Geosci. Remote Sens.*, *24*, 863–872.

Lyzenga, D. R. (2002), Unconstrained inversion of waveheight spectra from SAR images, *IEEE TGARS*, *40*, 261–270.

Mastenbroek, C., and C. F. de Valk (2000), A semiparametric algorithm to retrieve ocean wave spectra from synthetic aperture radar, *J. Geophys. Res.*, *105*, 3497–3516.

Phillips, O. M. (1985), Spectral and statistical properties of the equilibrium range in wind-generated gravity waves, *J. Fluid Mech.*, *156*, 505–531.

Rodgers, C. D. (2000), *Inverse Methods for Atmospheric Sounding: Theory and Practice*, *Ser. Atmos. Oceanic Planet. Phys.*, vol. 2, World Sci., Hackensack, N. J.

Schmidt, R. (1995), Bestimmung der Ozeanwellen-Radar-Modulations-Übertragungsfunktion aus der Abbildung des Ozeanwellenfeldes durch flugzeuggetragene Radarsysteme mit synthetischer Apertur, Ph.D. thesis, Univ. Hamburg, Germany.

Schulz-Stellenfleth, J., and S. Lehner (2002), Spaceborne synthetic aperture radar observations of ocean waves traveling into sea ice, *J. Geophys. Res.*, *107*(C8), 3106, doi:10.1029/2001JC000837.

Schulz-Stellenfleth, J., and S. Lehner (2004), Measurement of 2-d sea surface elevation fields using complex synthetic aperture radar data, *IEEE Trans. Geosci. Remote Sens.*, *42*, 1149–1160.

Schulz-Stellenfleth, J., and S. Lehner (2005), A noise model for synthetic aperture radar look cross spectra acquired over the ocean, *IEEE Trans. Geosci. Remote Sens.*, in press.

Schulz-Stellenfleth, J., S. Lehner, and D. Hoja (2002), Use of the coherence of synthetic aperture radar look cross spectra for ocean wave measurements, paper presented at the International Geoscience and Remote Sensing Symposium, Toronto, Canada.

D. Hoja and J. Schulz-Stellenfleth, Remote Sensing Technology Institute, German Aerospace Center (DLR), Oberpfaffenhofen, D-82234 Wessling, Germany. (johannes.schulz-stellenfleth@dlr.de)

S. Lehner, Rosenstiel School of Marine and Atmospheric Sciences, University of Miami, 4600 Rickenbacker Causeway, Miami, FL 33149, USA. (susanne.lehner@dlr.de)